Polarimetry-based tumor segmentation for pancreatic cancer using film-covered hematoxylin-and-eosin-stained slides

Davide Scandella[a], C. H. Lucas Patty[a,b], Paulo Sampaio[a], Heather DiFazio[a], Pablo Marquez Neila[a], Martin Wartenberg[c], Federico Storni[d], Brice Demory[a,b], Daniel Candinas[d], Aurel Perren[c], and Raphael Sznitman[a]

[a]ARTORG Center, University of Bern
[b]Center for Space Habitability, University of Bern
[c]Institute of Tissue Medicine and Pathology, University of Bern
[d]Department of Visceral Surgery and Medicine, Bern University Hospital

ABSTRACT

Mueller matrix polarimetry (MMP) has been shown to provide additional tissue information, including collagen alignment, structural heterogeneity, and stromal organization, compared to conventional imaging of histopathological slides. While previous studies have primarily used slides covered with glass coverslips, film coverslipping has become the standard due to its cost-effectiveness and improved long-term tissue preservation. However, the use of such slips introduces birefringence that potentially can affect MMP results. This raises the question of whether these spurious signals limit the ability of MMP to extract clinically relevant information from tissue covered with film. In this study, we employ deep learning to assess the feasibility of using MMP on film-covered slides, demonstrating its potential for medical applications.

80 hematoxylin-eosin (H&E) stained pancreatic tissue slides were imaged using a bespoke Mueller Matrix polarimeter operating in backscatter at zero degree phase angle in the following spectral ranges: $450 \pm 10\ nm$, $525 \pm 25\ nm$, $575 \pm 25\ nm$, $625 \pm 25\ nm$, $635 \pm 10\ nm$, $675 \pm 25\ nm$. The system ensured minimal added birefringence resulting from the polymer coverslip, allowing for consistent imaging at a resolution of 19 μm per pixel at 575 nm. A deep learning U-Net model was trained for the task of tumor segmentation using five-fold cross-validation, stratifying by tumor occurrence, and grouping by patients. The model achieved an area under the curve (AUC) of 0.97, an average precision (AP) of 0.83, and an intersection over union (IoU) of 0.69.

The results highlight the feasibility of extracting polarization signals from archival slides with resin-based coverslips and linking them to clinically relevant indications. This lays the foundation for the high-throughput digitization of vast slide repositories, facilitating the development of models that predict clinically relevant molecular biomarkers from more accessible MMP images. Hence, this approach holds significant potential to expand AI-driven diagnostics and advance the application of polarization imaging in oncology.

Keywords: Polarimetry, Mueller Matrix, Deep Learning, HE Slides

1. INTRODUCTION

Histopathology remains an integral part for diagnosing and characterizing pancreatic ductal adenocarcinoma (PDAC), one of the most aggressive malignancies with a poor prognosis.[1,2] Tissue sections from formalin-fixed, paraffin-embedded (FFPE) are typically stained with H&E and mounted on slides for microscopic evaluation by trained pathologists. This process enables detailed visualization of cellular morphology, nuclear atypia, and the prominent desmoplastic stroma characteristic of PDAC, features essential for accurate disease identification, grading, and therapeutic decision-making.[3]

An important step in slide preparation is the coverslipping used to fix the tissue material to the slide. This process can significantly influence image quality, scanning efficiency, and long-term preservation of slides.[4,5] Two main coverslipping techniques are widely used in pathology laboratories: (1) glass coverslipping, where a thin

---

Further author information: E-mail: davide.scandella@unibe.ch

Applications of Machine Learning 2025, edited by Michael E. Zelinski, Tarek M. Taha, Barath Narayanan
Abdul A. S. Awwal, Khan M. Iftekharuddin, Proc. of SPIE Vol. 13606, 1360613
2025 Published by SPIE · 0277-786X · doi: 10.1117/12.3064270

glass coverslip is manually applied over the slide using a mounting medium, and (2) film coverslipping, which uses a xylene-activated polymer film applied automatically.[6] For simplicity, these will be referred to as glass-covered and film-covered slides, respectively, throughout this study.

Film-covered slides have emerged as a promising alternative to traditional glass coverslips due to several operational and diagnostic advantages. Previous studies[7,8] have shown that film coverslipping reduces whole slide image (WSI) production time, decreases file sizes, and minimizes artifacts such as air bubbles and staining inconsistencies. Its automated application streamlines laboratory workflows and reduces variability, factors that are critical in high-throughput digital pathology environments. Moreover, film slides demonstrate superior long-term stability and reproducibility, making them increasingly popular in clinical routine and archival storage.[8]

Beyond their utility in standard microscopy and digital imaging, H&E-stained slides provide a rich substrate for advanced optical imaging modalities such as Mueller matrix polarimetry (MMP). MMP is a label-free technique that characterizes how polarized light interacts with tissue, capturing subtle changes in birefringence, depolarization, and scattering.[9] By analyzing the full Mueller matrix – a $4{\times}4$ matrix describing the polarization-altering properties of a sample – this method yields quantitative information about tissue microstructure, including collagen fiber orientation, density, and organization.[10] These features are particularly relevant in desmoplastic tumors like PDAC, where stromal architecture plays a key role in disease progression and prognosis.[11] Polarimetry thus offers unique contrast mechanisms sensitive to tissue microstructure, particularly the organization and alignment of collagen fibers in the tumor microenvironment.[12,13] These polarization properties have shown promise as a quantitative biomarker for tumor detection and prognosis in pancreatic cancer.

Despite the abundance of histological studies, bridging these findings to fresh tissue applications remains a critical step toward clinical translation. Indeed, a major challenge is in overcoming different backscattering effects due to slides and materials imaged. Encouragingly, Liu *et al.* (2018)[14] showed that retardance-derived polarimetric contrasts are consistent across both transmission-based imaging of stained slides and backscattering geometries used in fresh tissue diagnostics, indicating that polarimetric features obtained from FFPE slides can inform in vivo or ex vivo applications. Thin-film substrates commonly used in microscopy, however, introduce additional birefringence and depolarization that could alter polarimetric measurements.[15] Huang *et al.* (2021)[16] addressed this challenge by developing calibration and correction methods that mitigate artifacts arising from the plastic film, enabling the quantitative recovery of tissue polarization signatures even through these protective layers.

Along with these research directions, this work establishes a methodological foundation for applying MMP to film-covered slides, a prerequisite for integrating polarimetry with modern routine pathology workflows. Specifically, our goal is to achieve robust MMP imaging of standard slides with H&E staining such that complex tissue differentiation can be achieved from MMP data. Here, our objective is to demonstrate that pancreatic tumor tissue can be automatically identified. To do this, we present here a novel MMP system and a custom deep learning segmentation method capable of systematically and efficiently acquiring MMP data from film-covered H&E slides. We validate our approach on a dataset of collected PDAC slides and demonstrate high segmentation performance in terms of accuracy.

2. MATERIALS AND METHODS

2.1 Dataset

2.1.1 Histopathology pipeline

All tissue samples were collected at the Institute of Tissue Medicine and Pathology of the University of Bern, with approval from the Cantonal Ethics Committee of Bern (IRB no.: BE-2024-00553), in accordance with the Declaration of Helsinki. Samples originated from pancreaticoduodenectomies performed at the Department of Visceral Surgery, Bern University Hospital. Eligibility was limited to individuals aged 18 years and older who had signed institutional general consent. Patients with prior neoadjuvant therapy were excluded from the present work.

FFPE tissue blocks were sectioned and stained with H&E following standard clinical protocols. All slides were prepared on Superfrost® Plus glass substrates (Thermo Fisher Scientific, USA) and coverslipped using

Tissue-Tek® mounting film (Sakura Finetek, USA). The resulting H&E-stained sections include representative areas of pancreatic tissue, with a focus on regions relevant for histopathological assessment of PDAC. Table 1 summarizes the cohort composition, detailing the number of patients and H&E slides included in the study, along with the distribution of tumor tissue.

Table 1. Summary of the study cohort and slide distribution. The table reports the number of patients and FFPE H&E slides included in the study, along with the number of patients and slides containing tumor tissue.

	Total	Non-cancer	Cancer
H&E Slides	80	58	22
Patients	37	22	15

2.1.2 Sample gold standard annotation

The gold-standard annotations, consisting of segmentation masks, were provided by an experienced gastrointestinal pathologist. Annotations were performed directly on top of high-resolution WSIs using specialized digital pathology software. All regions exhibiting PDAC or associated desmoplastic stroma were annotated as tumor, constituting the positive class. All other regions, such as normal parenchyma, adipose tissue, blood vessels, and inflammatory infiltrates, were labeled as non-tumoral tissue, representing the negative class. Areas deemed clearly non-diagnostic or not pathologically relevant (e.g., extensive fat tissue) were excluded from annotation due to the significant manual effort required. As a result, a post-processing step was necessary to align and register the provided ground truth annotations with the corresponding imaging data for use in model training. Details regarding this post-processing procedure are presented in Section 2.3.

2.2 Mueller matrix polarimeter

The imaging Mueller matrix polarimeter was built in-house at the University of Bern. A diagram of the setup is presented in Figure 1.

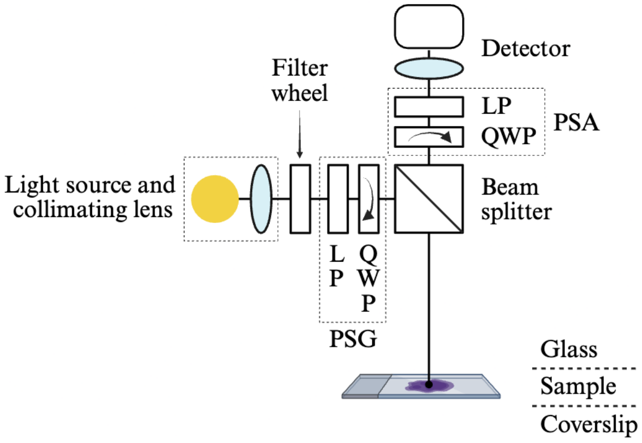

Figure 1. Schematic representation of the rotating retarding Mueller matrix ellipsometer setup in reflection, where PSG = polarization state generator, PSA = polarization state analyzer, LP = linear polarizer and QWP = quarter waveplate. The slides are positioned in front of the device with the glass surface facing the detector and the coverslip oriented away from it.

All measurements were carried out in reflection at zero-phase angle by means of a non-polarizing beam splitter plate. The system was calibrated in transmission and validated using phase retarders. The instrument is based on the commonly used dual-rotating-retarder concept as first described by Azzam.[17] A white LED optical source (MCWHLP3, Thorlabs, USA[*]) was placed in front of a collimator and a filter wheel with six

---

[*] Any mention of commercial products within this paper is for information only; it does not imply recommendation or endorsement by the authors or their affiliated institutions.

bandpass filters installed: 450 ± 10 *nm* (FBH450-10, Thorlabs, USA), 525 ± 25 *nm* (#86-951, Edmund Optics, UK), 575 ± 25 *nm* (#86-952, Edmund Optics, UK), 625 ± 25 *nm* (#86-953, Edmund Optics, UK), 635 ± 10 *nm* (FLH635-10, Thorlabs, USA), 675 ± 25 *nm* (#86-954, Edmund Optics, UK). Following this setup were a micro-controlled mechanical shutter and a polarization state generator (PSG). The light, after being reflected by the beam splitter plate (BSW10R, Thorlabs, USA), interacted with the sample before passing once more through the beam splitter and subsequently through the polarization state analyzer (PSA). A 55-mm telecentric focal length objective (f/2.8 TEC-55, Computar, Japan) then focused the light onto a 5 million pixel CMOS (Alvium 1800 U508m, Allied Vision, Germany) with a total spatial resolution of $19\mu m$ per pixel. Both the PSG and the PSA consisted of a fixed linear polarizer (LP) (WP25M-VIS, Thorlabs, USA) and a rotating quarter-wave plate (QWP) (RAC 3.4.20, B. Halle, Germany). The QWPs were mounted on a rotation stage (ELL14, Thorlabs, USA). As part of the calibration procedure, the beam splitter was characterized for both its transmission and reflection properties. These measured functions were subsequently incorporated into the system's measurement model, allowing accurate matrix multiplication during data analysis. Additionally, the exposure time was optimized individually for each wavelength, ensuring that the signal-to-noise ratio (SNR) remained approximately consistent across the spectral range.

During measurement, H&E-stained slides were placed in front of the optical detector with the plain glass slide surface facing the detector and the coverslip positioned on the opposite side, ensuring that the coverslip remained at the rear relative to the detection optics. This orientation was chosen to minimize the contribution of birefringence from the coverslip.

2.3 Data processing

The raw Mueller Matrix (MM) data were first normalized by dividing each of the 4 x 4 MM elements by the corresponding M_{11} element, on a per-pixel and per-wavelength basis, in order to decouple polarization properties from overall scalar intensity variation. The validity of the resulting normalized MM was assessed following established criteria for physical realizability and consistency.[18,19] Only regions with sufficiently strong signals were retained for further analysis; specifically, pixels were retained if their intensity reached at least 20% of the camera's full well capacity during acquisition. All other pixels were masked by setting all 16 MM elements to zero and excluding them from the segmentation mask. The same procedure was applied to overexposed pixels, *i.e.* beyond 85% of the camera full well capacity.

As illustrated in Figure 2, the normalized MMs were manually registered to the ground truth segmentation masks using *BigWarp*,[20] an interactive, landmark-based image registration tool, to enable supervised model training. A similarity transformation was applied during alignment. For each annotated sample, a bounding box was defined by extending the mask by 100 pixels in all directions, ensuring complete tissue coverage. A full-resolution binary mask was then generated, assigning a value of 1 to tumor pixels and 0 to non-tumoral tissue. Mask pixels were assigned a constant value of 100 to indicate background when they fell outside the annotated tissue regions, exhibited low SNR, or were overexposed. These background pixels were excluded from the loss computation during training.

2.4 Segmentation model and training

We cast the tissue identification problem as a semantic segmentation task, where the objective is to classify each pixel as either being cancerous or non-cancerous. To this end, we employed a U-Net-based convolutional neural network,[21] which takes as input multi-channel images derived from MM data and outputs a binary segmentation mask. The input consisted of 90 polarization features per pixel, corresponding to 15 normalized MM elements across 6 wavelengths, excluding M_{11}, which is always unity post-normalization.

As illustrated in Figure 3, the network adopts a standard U-Net architecture with an encoder–decoder structure and symmetric skip connections. The encoder comprises convolutional blocks with channel depths of 64, 128, and 256, leading to a bottleneck with 512 channels. The decoder mirrors this structure with transposed convolutions and feature concatenation. A final 1×1 convolution reduces the output to two channels corresponding to class logits, followed by a softmax activation for pixel-wise classification. The model was trained using a cross-entropy loss function, configured to ignore background pixels.

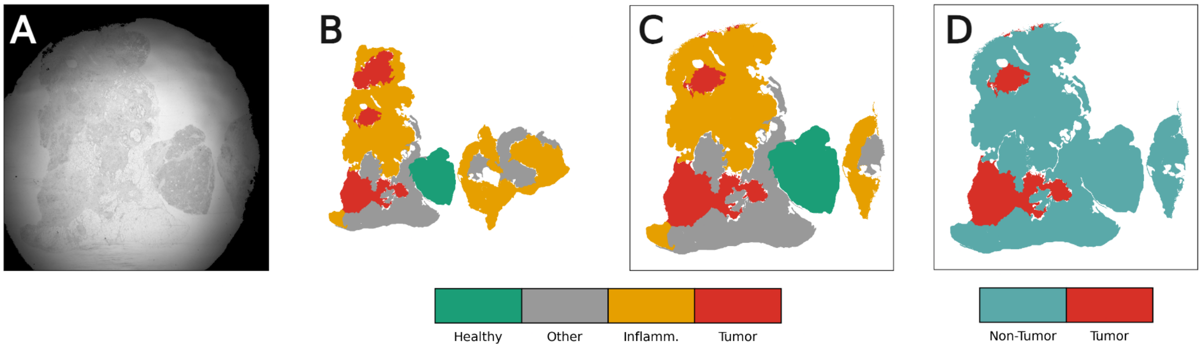

Figure 2. (A) Reference intensity image acquired at 625 nm. A 100-pixel margin is added around the sample, and pixels with weak signal (< 20% of camera well depth) are discarded (shown in black). (B) Detailed annotation mask created by the pathologist from the WSI. (C) Pathologist's annotation mask registered to the acquired image shown in A. (D) Binary annotation mask derived from C, where all non-tumor regions are merged into a single *Non-Tumor* label.

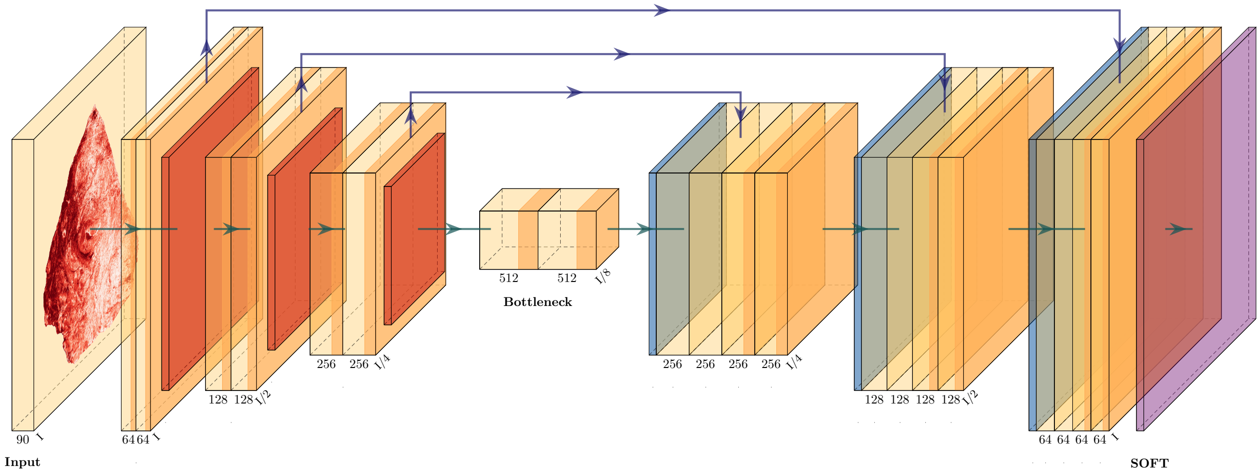

Figure 3. Schematic representation of the U-Net architecture employed in this study.

Due to variability in input image sizes, training was performed with a batch size of 1. We used stratified 5-fold cross-validation at the patient level to ensure a balanced representation of tumor and non-tumor cases across all splits. Table 2 shows the resulting distribution of patients, H&E slides, and pixels across folds, which reflects the hierarchical sparsity of tumor presence: not all slides from tumor-positive patients contain tumor, and even when present, tumor regions often occupy only a small portion of the slide.

The model was optimized using the Adam optimizer with a learning rate of 10^{-4}, and trained for a fixed number of 400 epochs. Implementation was carried out using PyTorch Lightning. Model performance was evaluated using several metrics, including AUC, IoU (also known as the Jaccard index), area under the precision-recall curve (or average precision, AP), F1 score, precision, recall, and specificity. The segmentation threshold was selected on a per-fold basis to maximize the IoU score.

3. RESULTS AND DISCUSSION

3.1 Mueller matrix measurements

Figure 4 presents the measured MMs from a representative H&E-stained FFPE slide of pancreatic tissue selected from the dataset. Subfigure 4A shows the full MM acquired with our instrument, as detailed in Section 2.2. The

Table 2. Summary of the study cohort, slides, and pixel distribution across folds.

	Patients	Patients with tumor	H&E slides	H&E slides with tumor	Pixels [M]	Pixels with tumor [M]
Fold 0	6	3 [50%]	17	5 [29%]	11.7	1.2 [10%]
Fold 1	7	4 [57%]	17	5 [29%]	14.7	1.8 [12%]
Fold 2	9	3 [33%]	15	4 [27%]	14.6	3.4 [23%]
Fold 3	9	3 [33%]	16	4 [25%]	13.1	3.5 [27%]
Fold 4	6	2 [33%]	15	4 [27%]	12.9	1.3 [10%]
Total	37	15 [41%]	80	22 [28%]	67.0	11.2 [17%]

resulting matrix exhibits clear perturbations due to the presence of the plastic film coverslip, consistent with prior observations.[16] However, an important distinction from previous work lies in the measurement geometry: while earlier studies primarily employed transmission-mode configurations, our data were acquired in backscattering mode, which resembles more closely conventional fresh tissue imaging setups used in ex vivo and in vivo contexts.

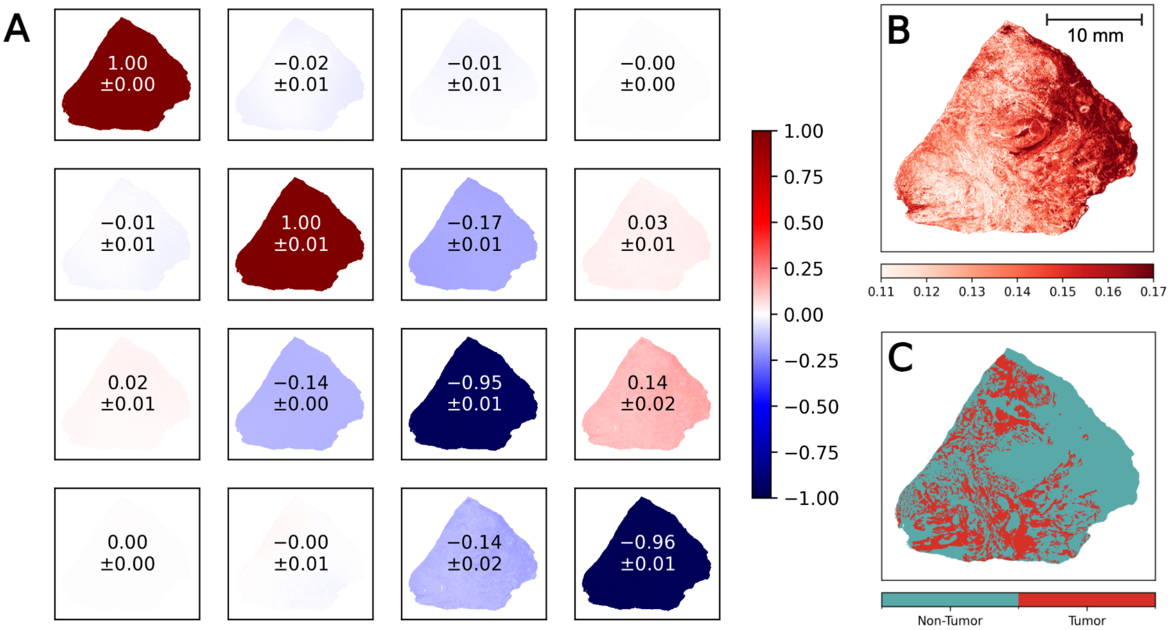

Figure 4. (A) Normalized Mueller matrix of a representative sample, with all matrix elements displayed using a fixed color scale ranging from −1 to 1. (B) Contrast-enhanced view of element $M_{3,4}$, obtained by adjusting the color scale to highlight subtle structural features within the sample. (C) Corresponding binary mask indicating tumor (red) and non-tumor (blue) regions, used as ground truth for segmentation.

A closer view of the MM element $M_{3,4}$ is shown in Figure 4B, highlighting localized spatial variations. Figure 4C displays the tumor segmentation mask related to the same region. Notably, regions with elevated or structured changes in $M_{3,4}$ appear to align with tumor areas in the corresponding segmentation map. Given the inherent antisymmetry of certain off-diagonal Mueller matrix elements ($e.g.\ M_{ij} = -M_{ji}$) for reciprocal systems under ideal conditions, similar patterns are also observed in $M_{4,3}$, suggesting that these elements may serve as robust markers for tumor presence. The observed antisymmetry arises from the reciprocity of light propagation in passive, non-magnetic materials.

These results indicate that certain off-diagonal elements of the Mueller matrix, particularly those capturing circular-linear polarization coupling (e.g., $M_{3,4}$ and $M_{4,3}$), could serve as effective proxies for tumor segmentation in H&E-stained pancreas tissue.

3.2 Tumor segmentation performance

Figure 5 shows the performance of our U-Net segmentation model trained to identify tumor regions. The model was evaluated using 5-fold cross-validation and the results are reported as mean ± standard deviation computed across the folds.

Figure 5A presents the receiver operating characteristic (ROC) curve, while Figure 5B displays the precision–recall curve. The model achieved strong performance, with an AUC of 0.967 ± 0.020, AP of 0.834 ± 0.155, and an IoU of 0.688 ± 0.152. Additional metrics include a precision of 0.790 ± 0.127, recall of 0.844 ± 0.148, specificity of 0.955 ± 0.035, and F1-score of 0.807 ± 0.104, evaluated at the optimal threshold of 0.266 ± 0.164.

These results demonstrate that MM data obtained from archival FFPE slides with film coverslips contain sufficient diagnostic contrast to support accurate tumor segmentation, despite the known optical distortions introduced by the overlay.

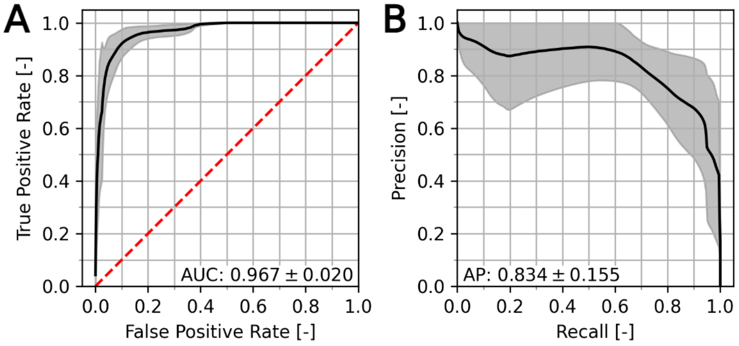

Figure 5. Pixel-wise segmentation performance metrics across cross-validation folds. In both plots, the mean is shown along with a gray band indicating the standard deviation. (a) ROC AUC computed per pixel. The red dotted diagonal line at AUC = 0.5 indicates the performance of a random classifier. Mean and standard deviation values are reported below the axis. (b) Precision-recall (PR) curve with corresponding mean and clipped standard deviation across folds. Following established practices in PR curve analysis,[22,23] standard deviation bands were clipped to the [0, 1] range to ensure consistency with the valid range of each metric.

3.3 Ablation study

3.3.1 Spectral band importance

To examine the effect of spectral content on segmentation performance, we performed an ablation study in which the MM data corresponding to each of the six bandpass filters was considered independently. Figure 6 summarizes the model's AUC (6A), AP (6B), and IoU (6C) when trained using all spectral bands (baseline) and each individual band alone.

The results indicate that the 625 ± 25 nm band yielded the best performance across all metrics, followed by the 575 ± 25 nm and the 635 ± 10 nm bands. In contrast, the 450 ± 10 nm band provided the poorest performance, with the 675 ± 25 nm also underperforming. These findings suggest that bands in the 550–650 nm range carry the most discriminative tissue information for polarimetric tumor segmentation, while the full-width at half maximum (FWHM) of the filters appears to play a lesser role compared to the choice of central wavelength.

3.3.2 Mueller matrix element importance

We evaluated the contribution of different subsets of Mueller matrix elements to segmentation performance. Figure 7 summarizes this analysis: AUC (7A), AP (7B), and IoU (7C) are shown for each configuration, with the matrix element configurations defined in Figure 7D.

Seven configurations were tested: (1)All MM elements (baseline); (2) Linear interaction block (upper-left 3×3 submatrix); (3) Circular interaction terms (last row and column); (4) Depolarization terms (diagonal elements);

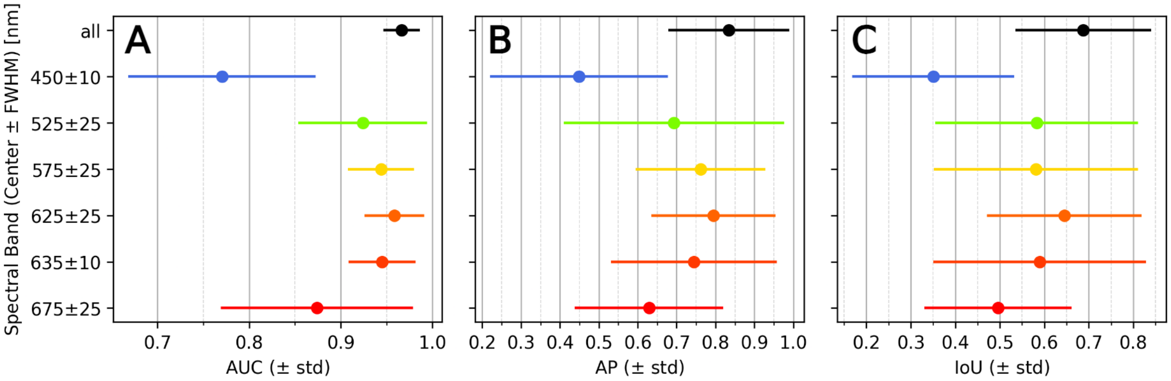

Figure 6. Ablation study showing segmentation performance across individual spectral bands. Each plot reports the performance of the model when using all spectral bands (uppermost point) versus each single band independently. Metrics shown are (A) AUC, (B) AP, and (C) IoU. Each point represents the mean performance across cross-validation folds, with horizontal error bands indicating standard deviation. FWHM = full-width at half maximum

(5) Polarization conversion terms (off-diagonal); (6) Circular–linear interaction block ($M_{2,4}$, $M_{3,3}$, $M_{3,4}$, $M_{4,2}$, $M_{4,3}$, $M_{4,4}$); (7) Linear birefringence ($M_{3,4}$, $M_{4,3}$), based on findings from Figure 4.

As expected from the initial analysis, configurations including depolarization terms and linear interaction blocks (Configs 2 and 4) resulted in the weakest performance. In contrast, Config 7 – focused on linear birefringence elements – achieved the best performance, closely matching or exceeding the full MM baseline. All configurations that were supersets of Config 7 performed similarly well, reinforcing the critical role of these specific elements in tumor discrimination. These results suggest that MM acquisition protocols can be simplified without substantial performance loss by prioritizing specific matrix elements. This optimization would reduce the number of required acquisition states and computational resources for solving the MM, further improving practical deployment.

4. CONCLUSION

This study demonstrates that accurate pancreatic tumor segmentation is achievable using deep learning applied to MMP data acquired from film-covered, H&E-stained archival slides. Rather than assessing the influence of coverslipping or staining – topics already addressed in prior work – our focus was to test whether reliable polarimetric signals for tumor classification could be extracted under these conditions.

The results confirm that specific MMP elements, particularly those linked to linear birefringence, retain discriminative power even in the presence of film-induced artifacts. Despite the limited dataset, our model achieved strong segmentation performance, showing that archival FFPE slides can support quantitative polarimetric analysis for tumor detection.

By validating this approach on existing archival material, we establish a framework for high-throughput analysis of large retrospective slide repositories. This has significant implications for future studies aiming to bridge the gap between archival data and fresh tissue applications – particularly in contexts where access to polarimetric measurements during surgical resections remains limited. Additionally, our ablation studies point to possible simplifications in acquisition protocols, reducing both spectral and polarimetric dimensionality while preserving performance, thereby making future fresh tissue imaging more efficient and targeted.

ACKNOWLEDGMENTS

This work was supported by funding provided by the University of Bern, the Novartis Research Foundation FreeNovation grant, and the Fond'Action Contre le Cancer. Calculations were performed on UBELIX (https://www.id.unibe.ch/hpc), the HPC cluster at the University of Bern.

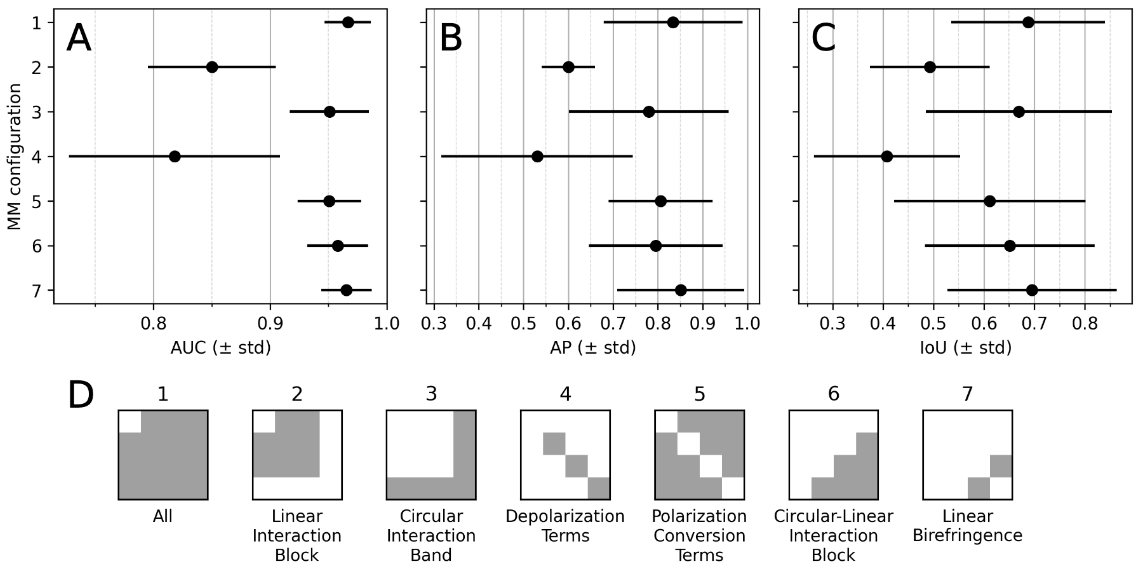

Figure 7. Ablation study showing segmentation performance across different MM subset configurations. Each plot reports the performance of the model when using all MM elements (uppermost point) versus each MM subset independently. Metrics shown are (A) AUC, (B) AP, and (C) IoU. Each point represents the mean performance across cross-validation folds, with horizontal error bands indicating standard deviation. (D) Configurations considered for the ablation study. M_{11} was excluded from all configurations.

REFERENCES

[1] Fu, H., Mi, W., Pan, B., Guo, Y., Li, J., Xu, R., Zheng, J., Zou, C., Zhang, T., Liang, Z., Zou, J., and Zou, H., "Automatic Pancreatic Ductal Adenocarcinoma Detection in Whole Slide Images Using Deep Convolutional Neural Networks," *Frontiers in Oncology* **11** (June 2021). Publisher: Frontiers.

[2] Yang, X., Jones, K., and Chen, G., "Pathology of Pancreatic Ductal Adenocarcinoma," in [*Hepato-Pancreato-Biliary Malignancies*], 483–517, Springer International Publishing (Jan. 2022).

[3] Basturk, O., Hong, S.-M., Wood, L. D., Adsay, N. V., Albores-Saavedra, J., Biankin, A. V., Brosens, L. A. A., Fukushima, N., Goggins, M., Hruban, R. H., Kato, Y., Klimstra, D. S., Klöppel, G., Krasinskas, A., Longnecker, D. S., Matthaei, H., Offerhaus, G. J. A., Shimizu, M., Takaori, K., Terris, B., Yachida, S., Esposito, I., Furukawa, T., and Baltimore Consensus Meeting, "A Revised Classification System and Recommendations From the Baltimore Consensus Meeting for Neoplastic Precursor Lesions in the Pancreas," *The American Journal of Surgical Pathology* **39**, 1730–1741 (Dec. 2015).

[4] Ravikumar, S., Surekha, R., and Thavarajah, R., "Mounting media: An overview," *Journal of Dr. YSR University of Health Sciences* **3**, S1 (Mar. 2014).

[5] Bancroft, J. D., [*Theory and Practice of Histological Techniques*], Elsevier Health Sciences (Jan. 2008). Google-Books-ID: Dhn2KispfdQC.

[6] Buesa, R. J., "Productivity standards for histology laboratories," *Annals of Diagnostic Pathology* **14**, 107–124 (Apr. 2010).

[7] Ferreira, D., Vale, J., Curado, M., Polónia, A., and Eloy, C., "The impact of different coverslipping methods in the quality of the whole slide images used for diagnosis in pathology," *Journal of Pathology Informatics* **13**, 100098 (May 2022).

[8] Retamero, J. A., Aneiros-Fernandez, J., and Del Moral, R. G., "Complete Digital Pathology for Routine Histopathology Diagnosis in a Multicenter Hospital Network," *Archives of Pathology & Laboratory Medicine* **144**, 221–228 (Feb. 2020).

[9] Ignatenko, D. N., Shkirin, A. V., Lobachevsky, Y. P., and Gudkov, S. V., "Applications of Mueller Matrix Polarimetry to Biological and Agricultural Diagnostics: A Review," *Applied Sciences* **12**, 5258 (Jan. 2022). Number: 10 Publisher: Multidisciplinary Digital Publishing Institute.

[10] Bancelin, S., Nazac, A., Ibrahim, B. H., Dokládal, P., Decencière, E., Teig, B., Haddad, H., Fernandez, H., Schanne-Klein, M.-C., and De Martino, A., "Determination of collagen fiber orientation in histological slides using Mueller microscopy and validation by second harmonic generation imaging," *Optics Express* **22**, 22561–22574 (Sept. 2014).

[11] Ray, A., Callaway, M. K., Rodríguez-Merced, N. J., Crampton, A. L., Carlson, M., Emme, K. B., Ensminger, E. A., Kinne, A. A., Schrope, J. H., Rasmussen, H. R., Jiang, H., DeNardo, D. G., Wood, D. K., and Provenzano, P. P., "Stromal architecture directs early dissemination in pancreatic ductal adenocarcinoma," *JCI Insight* **7**(3), e150330.

[12] Tumanova, K., Serra, S., Majumdar, A., Lad, J., Quereshy, F., Khorasani, M., and Vitkin, A., "Mueller matrix polarization parameters correlate with local recurrence in patients with stage III colorectal cancer," *Scientific Reports* **13**, 13424 (Aug. 2023). Publisher: Nature Publishing Group.

[13] KU, S., Kaniyala Melanthota, S., U, R., Rai, S., Mahato, K. K., and Mazumder, N., "Characterization and classification of ductal carcinoma tissue using four channel based stokes-mueller polarimetry and machine learning," *Lasers in Medical Science* **39**, 123 (May 2024).

[14] Liu, T., Sun, T., He, H., Liu, S., Dong, Y., Wu, J., and Ma, H., "Comparative study of the imaging contrasts of Mueller matrix derived parameters between transmission and backscattering polarimetry," *Biomedical Optics Express* **9**, 4413 (Aug. 2018).

[15] Slepkov, A. D., "Quantitative measurement of birefringence in transparent films across the visible spectrum," *American Journal of Physics* **90**, 625–634 (Aug. 2022). arXiv:2206.06983 [physics].

[16] Huang, T., Yao, Y., Pei, H., Hu, Z., Zhang, F., Wang, J., Yu, G., Huang, C., Liu, H., Tao, L., and Ma, H., "Mueller matrix imaging of pathological slides with plastic coverslips," *Optics Express* **31**, 15682 (May 2023).

[17] Azzam, R. M. A., "Photopolarimetric measurement of the Mueller matrix by Fourier analysis of a single detected signal," *Optics Letters* **2**, 148–150 (June 1978). Publisher: Optica Publishing Group.

[18] Cloude, S. R., "Conditions For The Physical Realisability Of Matrix Operators In Polarimetry," in [*Polarization Considerations for Optical Systems II*], **1166**, 177–187, SPIE (Jan. 1990).

[19] Simon, B. N., Simon, S., Mukunda, N., Gori, F., Santarsiero, M., Borghi, R., and Simon, R., "A complete characterization of pre-Mueller and Mueller matrices in polarization optics," *JOSA A* **27**, 188–199 (Feb. 2010). Publisher: Optica Publishing Group.

[20] Bogovic, J. A., Hanslovsky, P., Wong, A., and Saalfeld, S., "Robust registration of calcium images by learned contrast synthesis," in [*2016 IEEE 13th International Symposium on Biomedical Imaging (ISBI)*], 1123–1126 (Apr. 2016). ISSN: 1945-8452.

[21] Ronneberger, O., Fischer, P., and Brox, T., "U-Net: Convolutional Networks for Biomedical Image Segmentation," (May 2015). arXiv:1505.04597 [cs].

[22] Boyd, K., Eng, K. H., and Page, C. D., "Area under the Precision-Recall Curve: Point Estimates and Confidence Intervals," in [*Advanced Information Systems Engineering*], Hutchison, D., Kanade, T., Kittler, J., Kleinberg, J. M., Mattern, F., Mitchell, J. C., Naor, M., Nierstrasz, O., Pandu Rangan, C., Steffen, B., Sudan, M., Terzopoulos, D., Tygar, D., Vardi, M. Y., Weikum, G., Salinesi, C., Norrie, M. C., and Pastor, , eds., **7908**, 451–466, Springer Berlin Heidelberg, Berlin, Heidelberg (2013). Series Title: Lecture Notes in Computer Science.

[23] Clémençon, S. and Vayatis, N., "Nonparametric estimation of the precision-recall curve," in [*Proceedings of the 26th Annual International Conference on Machine Learning*], 185–192, ACM, Montreal Quebec Canada (June 2009).